Affordable membrane permeability calculations: Permeation of short-chain alcohols through pure-lipid bilayers and a mammalian membrane

Chi Hang Tse,[†] Jeffrey Comer,[‡] Simon Kit Sang Chu,[†] Yi Wang,[*,¶,†] and Christophe Chipot[*,§,‖,⊥]

†*Department of Physics, The Chinese University of Hong Kong, Shatin, Hong Kong SAR, China*

‡*Institute of Computational Comparative Medicine and Nanotechnology Innovation Center of Kansas State, Department of Anatomy and Physiology, Kansas State University, Manhattan, Kansas 66506*

¶*Shenzhen Research Institute, The Chinese University of Hong Kong, Shatin, Hong Kong SAR, China*

§*Laboratoire International Associé Centre National de la Recherche Scientifique et University of Illinois at Urbana-Champaign, Unité Mixte de Recherche n°7565, Université de Lorraine, B.P. 70239, 54506 Vandœuvre-lès-Nancy cedex, France*

‖*Theoretical and Computational Biophysics Group, Beckman Institute for Advanced Science and Technology, University of Illinois at Urbana-Champaign, 405 North Mathews Avenue, Urbana, Illinois 61801*

⊥*Department of Physics, University of Illinois at Urbana-Champaign, 1110 West Green Street, Urbana, Illinois 61801*

E-mail: yiwang@cuhk.edu.hk; chipot@ks.uiuc.edu

Abstract

Determination of membrane permeability to small molecules from first principles represents a promising approach for screening lead compounds according to their permeation properties upstream in the drug discovery process and prior to their synthesis. Theoretical investigation of permeation events requires, at its core, a molecular model of the membrane, and the choice of this model impacts not only the predicted permeability, but also its relation to the experimental measurements commonly performed in pharmaceutical settings with a variety of cell lines capable of mimicking intestinal passive permeation. Homogeneous single-lipid bilayers have traditionally been utilized in computer simulations of membrane permeability predictions due to the ease of sampling all the relevant configurations, as well as the availability of parameters for a range of components of the biological membrane. To assess the influence of the membrane heterogeneity on the permeability to small molecules, we have examined the permeation of ethanol in six different single-lipid bilayers, and compared the computed free-energy and diffusivity profiles with those obtained using a mammalian membrane model consisting of 26 components. Our results suggest that the membrane permeability only mildly depends on the lipid composition, spanning only one order of magnitude between the small phosphoethanolamine and the large phosphocholine head groups, or the short, saturated lauryl and the long, unsaturated oleyl acyl chains, that is, nearly as close as current theoretical estimates can get to experiment. The staggering computer time required to obtain an accurate free-energy profile, devoid of hysteresis between the upper and the lower leaflets of the lipid bilayer, in excess of several microseconds, provides an impetus for the development of approximate routes for membrane permeability predictions. Here, we have modeled the free-energy profile underlying permeation by means of a series of free-energy perturbation calculations, whereby the substrate is reversibly coupled to its environment at fixed values in the direction normal to the lipid bilayer. The diffusivity profile is modeled based on the bulk self-diffusion of the permeant and the membrane permeability is recovered without significant loss of accuracy. The proposed numerical approach can be seamlessly

extended to the determination of the relative membrane permeability to alternate substrates, thereby allowing large sets of permeants to be screened at a fraction of the computational cost of a rigorous determination of their respective free-energy profile.

1 Introduction

Lipid membranes are responsible for maintaining controlled chemical environments within all living cells and within their intracellular compartments. The hydrophobic core of these membranes acts as a free-energy barrier to many water-soluble species. Transport of most molecules and ions necessary for life is, therefore, tightly controlled by proteins integral to the membrane, such as channels and transporters. Nonetheless, passive diffusion is the dominant mechanism for membrane permeation of metabolic gases, e.g., dioxygen[1] and carbon dioxide,[2] signaling gases, e.g., nitric oxide[3] and hydrogen sulfide,[4] and endogenous steroids.[5] Small-molecule drugs and other exogenous substances may also enter cells by passive permeation. The relative importance of passive diffusion versus protein-facilitated transport remains, however, unclear in the general case, and, in all likelihood, stringently depends on the physicochemical properties of the molecule and the proteins present in the relevant membrane.[6–8] Hence, passive membrane permeability can be a crucial factor in the ability of drug candidates to reach intracellular targets, as well as for the determination of their intestinal absorption, and, to some extent, their oral availability. Recognizing poor membrane permeability early in the drug design process has the potential to reduce costs, especially if it can be achieved by means of computational methods, thereby, obviating the need to synthesize unpromising compounds.[9]

Molecular dynamics (MD) simulations can be used to accurately predict passive membrane permeability from the chemical structure of the permeant alone, while simultaneously revealing the mechanisms of permeation at the atomic scale.[10,11] The MD route to the estimation of membrane permeability was pioneered by Marrink and Berendsen,[12] leaning on the so-called solubility–diffusion model, whereby the free energy underlying permeation and

the diffusivity are hypothesized to continuously depend on the position of the permeant along a coordinate transverse to the membrane.[13]

In a nutshell, the reversible work incurred in the permeation process is calculated from the simulation as a function of the z–direction of Cartesian space, using one of the several importance-sampling algorithms available.[14,15] Some measure of the diffusion kinetics is estimated either from the same set of simulations used to evaluate the free energy, or from independent simulations. Conventionally, this measure is the position-dependent diffusion coefficient. However, we have recently developed a subdiffusion model based on a time-fractional diffusion equation, which appears to offer a better representation of the trajectories of the permeant derived from simulations.[16,17] It ought to be emphasized that the subdiffusive regime observed in our simulations stems in all likelihood from our rudimentary, however geometrically intuitive, description of the reaction coordinate by means of a simple projected Euclidean distance, evidently unable to capture the slowest degrees of freedom of the lipid bilayer known to contribute to the permeation events.[16]

To estimate the membrane permeability from first principles, employing numerical simulations, a molecular model must be chosen for the membrane. For simplicity, most theoretical investigations resort to bilayers composed of a single type of phospholipid. For instance, dipalmitoylphosphatidylcholine (DPPC) has been used in simulations aimed at determining the permeability of membranes to oxygen, ammonia and hydrogen sulfide,[18,19] as well as several small organic compounds.[20] In contrast to the fully saturated acyl chains of DPPC, a large proportion of lipids in mammalian membranes include one mono-unsaturated and one fully saturated tail,[21] e.g., 1-palmitoyl-2-oleoyl-glycero-3-phosphocholine (POPC). A number of computational studies have, therefore, used POPC to estimate membrane permeabilities to a variety of chemical species, like water,[22] oxygen,[23] short-chain alcohols,[16,17,24,25] nucleosides,[26] an arginine side-chain analogue,[27] as well as large pharmaceutical drugs.[28–30] Permeation of a capped tryptophan amino acid was studied in a 1,2-dioleoyl-sn-glycero-3-phosphocholine (DOPC) membrane,[31] which includes two unsaturations.

In recent years, more complex membrane models have emerged at an increasing pace in the pursuit of greater realism. Mammalian cell membranes typically include sizable concentrations of cholesterol, rationalizing the choice of mixtures of phospholipids and cholesterol in the earliest MD simulations of multicomponent bilayers.[32,33] On the other hand, atomic-scale models of the inner membranes of bacteria have been constructed based on mixtures of phosphatidylethanolamine and negatively charged phosphatidylglycerol lipids,[34] while a model of the stratum corneum incorporated ceramide lipids, cholesterol and free fatty acids.[35] The seminal work of Ingólfsson et al.[36] involved the construction of a coarse-grained model of a eukaryotic cell membrane consisting of 63 different lipid species and embodying a significant asymmetry in the compositions of the outer and inner leaflets. It is noteworthy that a web-based software, namely the CHARMM-GUI Membrane Builder, has been developed to allow atomistic membrane models composed of many components to be constructed easily.[37]

In the context of membrane permeability calculations, we recently determined the effect of cholesterol on the permeation of three drug-like molecules.[11] Although two of the compounds exhibited little change in their rates of permeation between a pure POPC bilayer and a POPC:cholesterol (2:1 mole ratio) bilayer, the permeability of the pure POPC membrane to the third compound, hydrocortisone, was more than two orders of magnitude higher than that of the POPC:cholesterol membrane. In another very recent investigation, permeation of cisplatin through a four-component model of a cancer-cell lipid bilayer was compared to that measured through a normal membrane.[38] Of particular interest, the model cancer cell membrane lacked the asymmetry between the inner and outer leaflet characteristic of the normal membrane, which translated to a significant decrease in permeability to cisplatin.

One important take-home lesson learned from over twenty years of theoretical investigations of permeation events is the necessity of sufficiently long MD simulations to average over fluctuations in the structure of the lipid bilayer, and, thus, obtain reliable results. Compared to bilayers consisting of a single type of lipid, multicomponent bilayers require far more simulation time to sample all thermodynamically favorable configurations. Enhanced sampling

techniques, including replica exchange,[?] can accelerate transitions between different lipid configurations.[39] Relaxation and sampling of multicomponent atomic-resolution membrane models remain, however, challenging. In the context of membrane permeability calculations, the situation is even more difficult, given that the internal degrees of freedom of the permeant[25,40] and the different positions of the permeant relative to the membrane must simultaneously be sampled. While many early computational studies were limited to multi-nanosecond simulations, obtaining convergence of the free-energy calculation to a precision significantly below the thermal energy, $k_{\mathrm{B}}T$ (where k_{B} is the Boltzmann constant and T, the temperature), requires sampling in excess of microseconds,[30] which currently corresponds to several days of continuous simulation on a modern workstation featuring graphics cards. In line with an earlier investigation, whereby tumbling of the permeant was considered explicitly in addition to the translation along the normal to the lipid bilayer,[25] the recent work by Sun et al. has demonstrated that multidimensional enhanced sampling can improve convergence.[30] However, rigorous MD–based calculations of permeability remain prohibitively expensive in terms of computational time to be used routinely in drug discovery.

In the present contribution, we seek to elucidate the influence of membrane composition on the permeation of a short-chain alcohol, while simultaneously demonstrating the applicability of a faster, more efficient and affordable approach to estimate membrane permeability from MD simulations. Toward this end, we apply MD and free-energy calculation techniques to six pure-lipid membranes, each consisting of a different lipid species, and a seventh asymmetric model of a mammalian membrane. We compare the free-energy and fractional diffusivity profiles produced with the different computational assays, and assess the effect of the membrane composition on its permeability. Earlier simulations have clearly shown that only small intervals of the the free-energy profile dominate the solubility–diffusion integral,[12] namely those regions of the highest free energy. In many cases,[28] it should, therefore, be possible to estimate with the suitable accuracy the membrane permeability without the need to determine the complete free-energy and diffusivity profiles. Here, we evaluate the ability

of free-energy perturbation[41,42] to supply the free energy at selected discrete points along the direction transverse to the membrane, and recover through interpolation the free-energy profile underlying permeation.

2 Methods

2.1 Theoretical Underpinnings

In this contribution, we focus on the estimation of the permeability of membrane models to a small molecule, which can be viewed as the evaluation of the net flux of the permeant across the membrane through integration over its thickness, i.e., $-L/2 \leq z \leq +L/2$, which forms the basis of the solubility–diffusion model for permeation. In the steady state, the resistance against permeation writes,

$$R := \frac{1}{P_{\mathrm{m}}} = \int_{-L/2}^{+L/2} \mathrm{d}z \, \frac{\exp[+\beta w(z)]}{D(z)} \tag{1}$$

where $\beta = 1/(k_{\mathrm{B}}T)$, and k_{B} is the Boltzmann constant and T, the temperature. $w(z)$ is the potential of mean force (PMF) underlying permeation, i.e., the reversible work incurred to translocate the substrate between the aqueous phases on each side of a lipid bilayer along z. $D(z)$ is the position-dependent classical diffusivity. As was demonstrated in an earlier contribution,[16] however, the non-Markovian behavior of permeation monitored along the naive reaction-coordinate model consisting of the z direction of Cartesian space, i.e., the normal to the lipid bilayer, cannot be adequately described by the solubility–diffusion model, which justifies turning to a fractional variation of the latter, i.e., replacing $D(z)$ by $K_\alpha(z)$, the position-dependent fractional diffusivity of fractional order α. $K_\alpha(z)$ is determined using a variant[16] of the Bayesian-inference scheme developed for Markovian models,[22,43,44] and implemented in the program DiffusionFusion.[44,45] While $K_\alpha(z)$ possesses different units than $D(z)$, P_{m} determined via Eq 1 with the former is numerically identical to that obtained via

solving the Smoluchowski equation with a concentration imbalance enforced between the two sides of the membrane.[16,17] Additionally, it is noteworthy that the membrane permeability, P_{m}, has no explicit dependence on the fractional order.

The trajectory of the permeant, $Z(t)$, and the PMF underlying permeation are readily obtained from a free-energy calculation with a time-dependent bias, as is the case with the ABF algorithm.[46] Starting with an initial guess of $K_\alpha(z)$ and $\alpha(z)$, the likelihood of the observed trajectory is given by,

$$P[Z(t)|K_\alpha(z),\alpha(z)] = \prod_j P[Z(t_j+\Delta t)|Z(t_j),K_\alpha(z),\alpha(z)] \tag{2}$$

where Δt is the time interval in the discretization scheme utilized for the trajectory of the permeant along z. The likelihood of the observed trajectory is the product of all the conditional probabilities of a displacement at time t_j, given the current estimate of $K_\alpha(z)$ and $\alpha(z)$. The objective of the Bayesian approach is to find $K_\alpha(z)$ and $\alpha(z)$ that maximize the posterior probability, $P[K_\alpha(z),\alpha(z)|Z(t)]$, which is connected to the likelihood through the Bayes theorem,[16]

$$P[K_\alpha(z),\alpha(z)|Z(t)] = P[Z(t)|K_\alpha(z),\alpha(z)]P_{\mathrm{prior}}[K_\alpha(z)] \tag{3}$$

This model introduces a prior, P_{prior}, which is the product of priors assuming scale invariance and smoothness of the diffusivity.[16] In the present fractional solubility-diffusion model, $P[Z(t_j+\Delta t)|Z(t_j),K_\alpha(z),\alpha(z)]$ is determined employing the Crank–Nicolson finite-difference algorithm,[47–49] and a first-order approximation of the fractional derivative.

2.2 Computational assays

Six single-lipid bilayers were investigated, using 1,2–dilauroyl–sn–glycero–3–phosphocholine (DLPC), 1,2–dilauroyl–sn–glycero–3–phosphoethanolamine (DLPE), 1,2–dimyristoyl–sn–glycero–3–phosphocholine (DMPC), DOPC, 1,2–dioleoyl–sn–glycero–3–phospho–L–serine (DOPS),

and 1–palmitoyl–2–oleoyl–sn–glycero–3–phosphoethanolamine (POPE). These lipids cover a variety of head groups and acyl-chain lengths, as listed in Table 1. Phosphatidylcholine (PC) and phosphatidylethanolamine (PE) lipids are electrically neutral, whereas phosphatidylserine (PS) is negatively charged. Figure S1 depicts the chemical structures of the six lipid species utilized in this work.

The mammalian membrane model features 26 components, comprising 25 lipid types, which includes phosphatidic acid (PA), PC, PE, PS and phosphatidylinositol (PI) lipids, as well as cholesterol (Table S1 and Figure S2). It is highly heterogeneous and asymmetric, owing to the distinct compositions in the upper and lower leaflets. Using the model of Ingólfsson, *et al.*[36] as a reference, we built the all-atom mammalian membrane with the CHARMM-GUI Membrane Builder.[37] The dimensions of the simulation box were approximately 80 Å×80 Å×100 Å. Lipids and cholesterol were distributed asymmetrically across this membrane, with a slightly different density for cholesterol between the two leaflets. The mammalian membrane model was equilibrated for 500 ns before an ethanol molecule was introduced into the simulation box. Overall, this asymmetric membrane revealed no apparent curvature arising from the compositional asymmetry.

Table 1: Details of the six single-species lipid bilayers studied in this work.

Bilayer	Headgroup	Tail length	Tail saturation
DLPC	phosphocholine	12:0	saturated
DLPE	phosphoethanolamine	12:0	saturated
DMPC	phosphocholine	14:0	saturated
DOPC	phosphocholine	18:1	unsaturated
DOPS	phosphoserine	18:1	unsaturated
POPE	phosphoethanolamine	16:0/18:1	mono-unsaturated

The six single-lipid bilayers were built using the CHARMM-GUI membrane builder.[37] The pure-lipid bilayers consisted of 50 lipid molecules per leaflet, in equilibrium with a water layer, about 22 Å thick. The final computational assays had an area in the x, y–plane of about 60×60 Å^2, and a dimension along the z–direction of Cartesian space ranging between 100 and 120 Å, which corresponds to 5,843–8,221 water molecules. In the case of the DOPS

bilayer, sodium ions were added to obtain electric neutrality.

For the mammalian membrane, the outer leaflet contained 89 lipid units and 38 cholesterol molecules, whereas the inner leaflet contained 86 lipid units and 43 cholesterol molecules. The initial dimensions of the mammalian membrane computational assay model were equal to $85 \times 85 \times 94$ Å^3 after hydration. Sodium and chloride ions were added to obtain electric neutrality and yield a 0.15 M ionic concentration.

2.3 Molecular dynamics simulations

All the MD simulations reported in this study were performed using NAMD 2.12,[50] using the CHARMM generalized force field (CGenFF) for the short-chain alcohols, the CHARMM36 force field for lipids[51] and the TIP3P water model.[52] A Langevin thermostat with a damping coefficient of 1 ps^{-1} maintained the temperature at 308 K. The Langevin piston method[53] was used to keep the computational assays at a nominal pressure of 1 atm. Covalent bonds involving hydrogen atoms were constrained to their equilibrium length with the Rattle algorithm.[54] The Settle algorithm was utilized to constrain water molecules to their equilibrium geometry.[55] Long-range electrostatic forces were evaluated employing the particle–mesh Ewald algorithm with a grid spacing of 1.2 Å, while a smoothed 9-Å spherical cutoff was applied to truncate short-range van der Waals and electrostatic interactions. The r–RESPA multiple time-stepping algorithm was employed to integrate the equations of motion with an effective time step of 2 fs for short-range interaction and 4 fs for long-range interactions.[56]

2.4 Free-energy calculations

To determine the PMF, $w(z)$, underlying the translocation of ethanol across the different lipid bilayers, the importance-sampling ABF algorithm[46] was employed. The free-energy profiles were determined by integration of the average force exerted along the transition coordinate,[57–59] defined as the projection onto the z–direction of Cartesian space, i.e., the normal to the membrane, of the Euclidean distance separating the center of mass of ethanol

from that of the lipid bilayer. The total permeation pathway spanned 90 Å, i.e., $-45 \leq z \leq +45$ Å. To enhance computational efficiency, the permeation pathway was broken down into nine windows, each 10 to 15 Å wide, and overlapping sequentially over 5 Å. In each window, the transition coordinate was discretized into bins 0.1 Å wide, in which samples of the local force acting along z were accumulated.[46]

As a preamble to each PMF calculation, an initial 100-ps equilibration in the isobaric–isothermal ensemble was performed prior to steered molecular dynamics (SMD) simulations, in which ethanol was pulled irreversibly from $z = -35$ to $+35$ Å across the lipid bilayer at a speed of 5 Å/ns, resulting in a total simulation time of 100 ns. From each SMD trajectory, nine configurations were extracted, corresponding to the nine initial positions of the permeant, i.e., $z = -35$, -30, -20, -10, 0, $+10$, $+20$, $+30$ and $+35$ Å. Each configuration was subject to a long equilibration of up to 100 ns (Table S1).

The uncertainty in $w(z)$ was estimated by considering the deviation of the gradients between the two halves of the trajectory in each window,[16] denoted as $g_s^1(z)$ and $g_s^2(z)$, respectively. The error of the final gradient is denoted as $\mathrm{Err}[g(z)] = \left|g_{\mathrm{sym}}^1(z) - g_{\mathrm{sym}}^2(z)\right|/2$, where $g_{\mathrm{sym}}^1(z)$ and $g_{\mathrm{sym}}^2(z)$ were obtained through anti-symmetrizing the gradients $g_s^1(z)$ and $g_s^2(z)$. The uncertainty at the edge of the simulation box was set to zero, i.e., $\mathrm{Err}[w(a)]=0$, where $a = \pm 45$ Å. The uncertainty of $w(z)$ originates from the integration of uncertain gradient values from the edge of the simulation box. Taking the assumption that the gradients at each value of z are statistically independent, the error associated to the PMF, $\mathrm{Err}[w(z)]$, was calculated from $\mathrm{Err}[g(z)]$ as:

$$\mathrm{Err}[w(z)] = \left| \int_a^z \mathrm{d}z' \, \mathrm{Err}[g(z')]^2 \right|^{\frac{1}{2}} \tag{4}$$

2.5 Modeling the free-energy landscape

As an alternative to the computationally intensive determination of the PMF underlying permeation, we modeled the latter by means of alchemical transformations, whereby the

permeant is reversibly coupled to its environment at fixed values of the transition coordinate. Creation and annihilation of ethanol were performed with the POPC computational assay, employing free-energy perturbation[41,42] (FEP) at five distinct positions along half of the permeation pathway, namely z = 0, 4, 13, 22 and 30 Å. Reversible coupling at each point was broken down into 20 strata, i.e., $\Delta\lambda = 0.05$, and the simulation time per stratum was 10 ns, including 0.5 ns of equilibration. The model PMF was recovered by interpolating the five free-energy values using a piecewise cubic Hermite interpolating polynomial.

To reduce further the cost incurred in membrane permeability estimation through mapping of the free-energy landscape that underlies permeation, we turned to the calculation of relative quantities, using FEP. The PMF for 1-propanol and 1-butanol was modeled through a sequence of point mutations, whereby ethanol was transformed into 1-propanol, and 1-propanol into 1-butanol. The thermodynamic cycle describing the series of mutations is depicted in Figure S3. Leaning on the PMF characterizing ethanol permeation through the POPC bilayer, we performed the alchemical transformations in both the bulk water and membrane environments. The PMF underlying 1-propanol permeation at a given value z, denoted as $w_{\mathrm{B}}(z)$, as illustrated in Figure S3, can be recovered from the knowledge of the PMF underlying ethanol permeation, $w_{\mathrm{A}}(z)$, at the same value of the transition coordinate:

$$w_{\mathrm{B}}(z) = w_{\mathrm{A}}(z) + \Delta G^{3}_{\mathrm{alch}} - \Delta G^{1}_{\mathrm{alch}} \tag{5}$$

In turn, the PMF underlying 1–butanol permeation, $w_{\mathrm{C}}(z)$, was inferred from the mutation of 1–propanol into 1–butanol in the aqueous and lipid environments, using FEP calculations:

$$w_{\mathrm{C}}(z) = w_{\mathrm{B}}(z) + \Delta G^{2}_{\mathrm{alch}} - \Delta G^{4}_{\mathrm{alch}} \tag{6}$$

2.6 Kinetic modeling

The position-dependent fractional diffusivity estimation, $K_\alpha(z)$, and the fractional order, $\alpha(z)$, were inferred from the ABF trajectories. For each of the nine windows forming the permeation pathway and the seven computational assays, we simultaneously optimized $K_\alpha(z)$ and $\alpha(z)$, using a Bayesian-inference scheme, whereby the trajectory of the permeant is discretized into sets of displacements over appropriate lag times, Δt. The lag time, Δt must be chosen long enough, so that the motion of the permeant is diffusional rather than ballistic.[16]

In this work, concomitantly with the computationally efficient approach put forth to interpolate the PMF based on a limited set of FEP calculations, we propose to approximate $K_\alpha(z)$. Five points are carefully chosen to represent the characteristic features of the fractional diffusivity profile, most notably the diffusivity plateau in the tail region and the bump at the center of the lipid bilayer. Additional points are included in the aqueous phase and in the hydrophobic core of the lipid bilayer using our knowledge of $K_\alpha(z)$ for a given type of lipid. The complete fractional diffusivity profile was then recovered by interpolating the estimate of K_α at the different values of z, employing a piecewise cubic Hermite interpolating polynomial.

3 Results and Discussion

3.1 Translocation free energy, diffusivity and permeability of single-lipid bilayers to ethanol

Using the ABF algorithm, we determined the free-energy profiles underlying permeation of ethanol through six single-lipid bilayers, namely, DLPC, DLPE, DMPC, DOPC, DOPS, and POPE. The aggregate simulation time for each system, shown in Table 2, spans the multi–μs timescale — roughly 2.4–4.5 μs. Convergence of our calculations was assessed

based on the free-energy difference between the aqueous phases above and below the lipid bilayer ($z = \pm 45$ Å), i.e., the hysteresis. All simulations were pursued until the hysteresis fell below $k_{\mathrm{B}}T$. Given that the two leaflets are identical in single-lipid bilayers, their free-energy profiles were then symmetrized by anti-symmetrizing the gradients (Figure 1). In the following analysis, we focus on three regions of the PMFs, namely the barrier region centered at $z = 0$, the interfacial peak around $z = \pm 20$ Å, and the interfacial valley around $z = \pm 10$ Å. The latter two regions reside above and below the lipid-water interface, corresponding to the local free-energy maxima and minima in the PMFs, respectively, i.e., the stationary points. The observation that the most favorable location for ethanol is near the water–lipid interface, most notably for PC lipids, is congruent with magic-angle spinning nuclear Overhauser enhancement spectroscopy data.[60]

Table 2: Simulation time (t) of the ABF calculations and the free-energy values ($w(z)$, unit: kcal/mol) at the peak and valley regions in each lipid bilayer. The width of the free-energy barrier is also provided, defined as the distance along z between the two points with half the peak $w(z)$ on the PMFs.

Bilayer	t (μs)	peak $w(z)$	valley $w(z)$	barrier width (Å)
DLPC	3.2	2.5	−0.2	6.2
DMPC	4.5	2.7	−0.3	9.1
DOPC	2.7	2.6	−0.4	14.7
DLPE	2.5	3.0	0.4	15.9
DOPS	3.6	2.9	−0.3	18.3
POPE	4.5	3.0	0.2	20.1
Mammalian	3.6	3.5	−0.2	23.8
Aggregate simulate time (μs)		**18.9**		

The free-energy barriers against ethanol permeation range from 2.5 to 3.0 kcal/mol among the six single-lipid bilayers examined here. Consistent with previous findings,[17,24] these values indicate that lipid bilayers do not present a huge barrier against the permeation of this short-chain alcohol. Overall, while the PMFs share similar features, both the height of the barrier and the width of its plateau are markedly different among the different lipid bilayers considered here. For instance, DLPC, which has the shortest (12-carbon) acyl chain and a relatively bulky head group, corresponds to the narrowest barrier, namely 6.2 Å wide

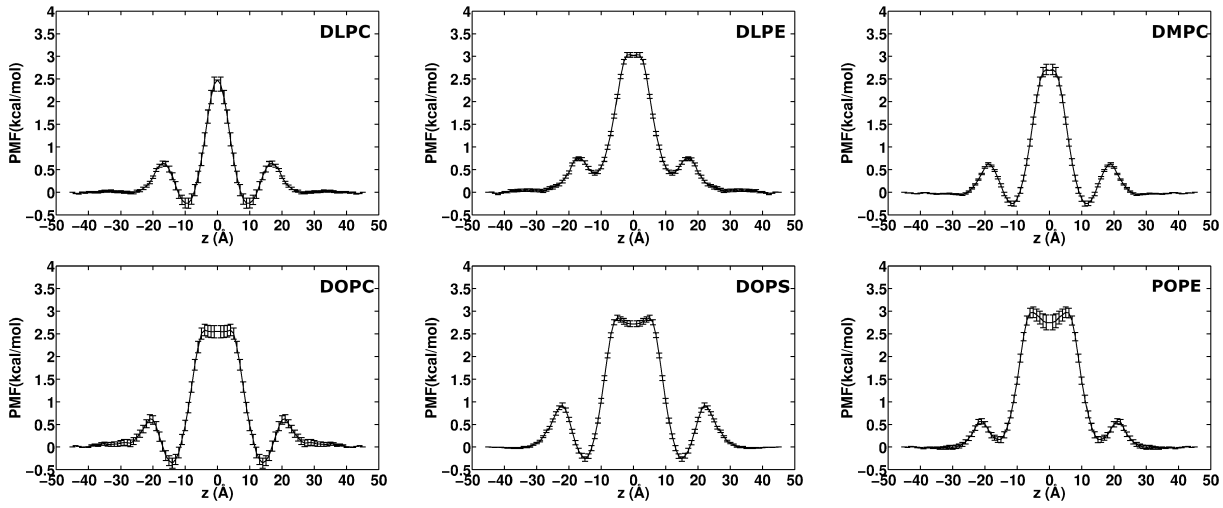

Figure 1: Free-energy profiles $w(z)$ for the permeation of ethanol in DLPC, DLPE, DMPC, DOPC, DOPS, and POPE. The transition coordinate z, represents the Euclidean distance between the center of mass of ethanol and the center of a lipid bilayer, projected onto the membrane normal. The error bars represent the estimated uncertainty of the free-energy for permeation of ethanol in membrane.

with the lowest height, i.e., 2.5 kcal/mol, whereas POPE, with the longest (18-carbon) acyl chain and a relatively small head group, has the widest plateau, i.e., 20.1 Å , and the highest barrier, i.e., 3.0 kcal/mol. Apart from the barrier regions in the PMFs, the interfacial peaks and valleys at the lipid-water interface also depend strongly on the lipid structure. For instance, DOPS, which possesses a negatively charged head group, corresponds to an interfacial peak of 1.0 kcal/mol, nearly 50% greater than those of the neutral PC lipids. Furthermore, the interfacial valley with DOPS is the most pronounced (≈1 kcal/mol from this valley to the interfacial peak), whereas for PE lipids, the depth of the valley is only around 0.2 kcal/mol.

The position-dependent fractional-diffusivity profiles, $K_\alpha(z)$, for ethanol permeating different lipid bilayers are shown in Figure 2. Just as the lipids with the longest acyl chains display the broadest PMF barriers, they also exhibit the widest regions of low diffusivity. These diffusivity profiles are qualitatively similar to our previous results on bulkier permeants[11], although a somewhat more pronounced bump is observed around $z = 0$ in bilayers with long lipid tails, namely, DOPC, DOPS and POPE. The values of $K_\alpha(z)$ far from the membrane,

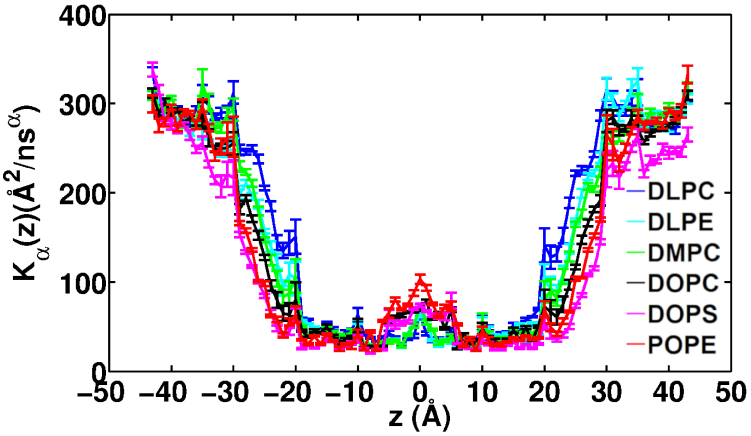

Figure 2: Position-dependent fractional diffusivities $K_\alpha(z)$ for DLPC, DLPE, DMPC, DOPC, DOPS, and POPE. The error bars are given by the width of the Bayesian posterior distribution, representing the uncertainty of diffusivities.

i.e., $|z| > 35$ Å, are consistent with independent simulations that measure the classical diffusivity of ethanol in bulk water. More specifically, using the Einstein–Smoluchowski formula, $D = \lim_{t\to\infty} \left\langle [\mathbf{r}(t) - \mathbf{r}(0)]^2 \right\rangle / 6t$, we found the bulk diffusivity of ethanol to be approximately 350 Å^2/ns, which agrees well with the values obtained in the bulk water regions of our membrane systems (Figure 2).

Based on the aforementioned PMFs and fractional-diffusivity profiles, the membrane permeability to ethanol was determined and reported in Table 3, along with the value obtained in a POPC bilayer by Comer and Chipot[17] for comparison. Overall, P_m varies by approximately an order of magnitude within the six single-lipid bilayers and mammalian membrane model. Robust experimental data against which our theoretical estimates can be compared are scarce. For instance, the controversial[24] measurement of Ly and Longo, using 1–stearoyl–2–oleoyl–phosphocholine,[61] is, contrary to chemical intuition, three orders of magnitude lower than the permeability of a POPC bilayer to water.[62] Equally surprising are the measurements of the membrane permeability in human red cells found to be nearly identical for water[63] and ethanol,[64] and both an order of magnitude lower than the permeability of a POPC bilayer to water.[62] Interestingly enough, the experimental permeabilities

to water of the lipid bilayers utilized in the present work were also found by Mathai et al.[62] to span an order of magnitude, DLPE being the least permeable and DOPC, the most permeable. At the computational level, following a strategy akin to ours, albeit with a distinct force field, Ghaemi et al.[24] estimated the permeability of a POPC bilayer to ethanol to be equal to 0.085 cm/s, i.e., an order of magnitude lower than ours. In general, P_{m} depends on both the lipid head group and tail structures. We discuss this dependence in more detail in the following section.

Table 3: Calculated membrane permeability, P_{m}, of various lipid bilayers to ethanol. The P_{m} value for POPC is taken from Comer and Chipot.[17]

Lipid Bilayer	P_{m} (cm/s)
DLPC	1.31 ± 0.08
POPC	0.81
DMPC	0.66 ± 0.05
DOPC	0.59 ± 0.03
DLPE	0.32 ± 0.02
DOPS	0.31 ± 0.01
POPE	0.29 ± 0.04
Mammalian	0.12 ± 0.01

3.2 Ethanol permeation across a mammalian membrane model

In addition to the six single-lipid bilayers described above, we examined the permeability to ethanol of a mammalian membrane model containing 25 lipid species and cholesterol. An all-atom system was constructed based on the coarse-grained (CG) mammalian membrane of Ingólfsson et al.[36] Given the limited size of our patch ($\approx 80 \times 80$ Å^2), not all lipid species from their CG membrane (in excess of 60) were included in our model. The resulting lipid mixture represents, to the best of our knowledge, the most sophisticated membrane model employed in atomistic permeability calculations to date. Following the same protocol followed for the single-lipid bilayers, we determined the PMF of ethanol permeation across the entire membrane, while keeping track of the free-energy difference between the two bulk water

regions as a measure of convergence. Given the heterogeneous, asymmetric nature of the membrane, its PMF was not symmetrized a posteriori, although the residual free-energy difference (∼0.3 kcal/mol) between the two bulk water regions was evenly spread over the final PMF.

The height of the free-energy barrier against ethanol permeation is 3.5 kcal/mol in the mammalian membrane. While this barrier is only slightly higher than that for the six single-lipid bilayers (2.5–3.0 kcal/mol), its width (23.8 Å) is significantly larger than that of the other bilayers. Overall, the mammalian membrane exhibits the greatest resistance to ethanol permeation among all systems studied here (Table 3). Its P_{m} value of 0.12 cm/s is approximately an order of magnitude smaller than that of the most permeable DLPC bilayer. Out of the six single-lipid bilayers, P_{m} for the POPE bilayer best mimics that of the mammalian membrane, with the former representing an approximately two-fold overestimation of the latter. This result is explained by the fact that the form of the PMF of the POPE bilayer most closely mimics that of the mammalian membrane, both in terms of the barrier height and width, as well as the amplitudes of the interfacial peaks and valleys. Interestingly enough, the value of P_{m} reported previously for the POPC bilayer[17] (0.81 cm/s) deviates significantly from that of the POPE bilayer and the mammalian membrane. Considering that PC lipids are the most abundant phospholipid species in a mammalian membrane[65] and POPC is routinely used to construct model plasma membranes, this deviation may come as a surprise. Further analysis of lipid structural properties, as detailed below, indicates that this result can be largely explained by the presence of cholesterol, as well as various charged lipid species, which produce a more densely packed mammalian membrane, compared with a pure POPC bilayer.

3.3 Effect of the lipid structure on ethanol permeation

Despite the similarities in shape of the free-energy and diffusivity profiles for the six single-lipid bilayers studied here, our results underscore the influence of lipid structure on membrane

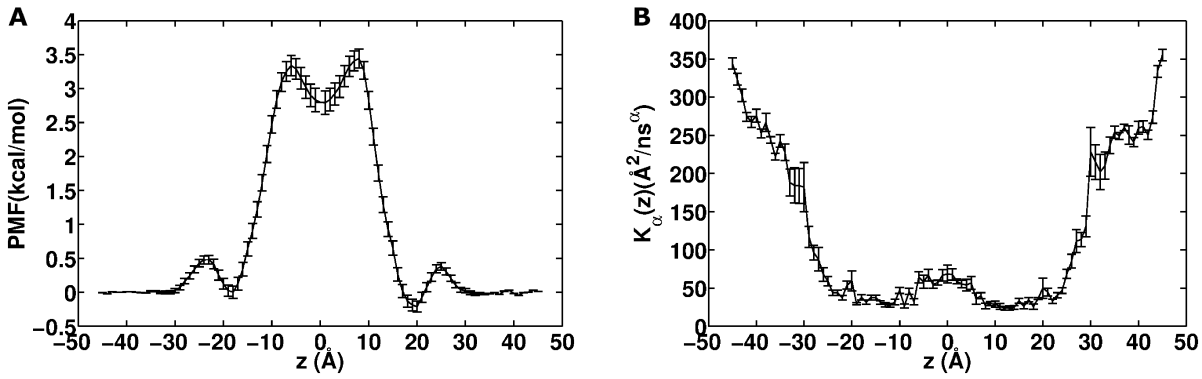

Figure 3: Free-energy profile $w(z)$ (A) and fractional diffusivity $K_\alpha(z)$ (B) for the permeation of ethanol in a mammalian membrane model. The error bars represent the estimated uncertainty of the free-energy and diffusivity for permeation of ethanol in the membrane.

permeability. To further analyze this influence, we determined the area per lipid (APL), electron density profile (EDP), tail-order parameter ($|S_{CD}|$), as well as the number of hydrogen bonds within each computational assay (Figure 4 and Table 4). Overall, for lipids possessing the same head group, a longer the tail is correlated with a broader free-energy barrier, which in turn produces a stronger resistance to permeation. Taking the PC lipids as an example — as the length of the acyl chain increases from 12 to 14 carbons, the permeability to ethanol drops from 1.3 (DLPC) to 0.66 cm/s (DMPC). Introducing unsaturation into the acyl chain, however, largely offsets, or even outweighs the effect of increased chain length, i.e., the unsaturated 18:1 DOPC and the mono-unsaturated 16:0/18:1 POPC have comparable, or even higher P_m than the saturated 14:0 DMPC.

Apart from their tails, the nature of the head group of the lipid molecules has a profound impact on P_m. Permeability to ethanol in lipids endowed with a phosphocholine head group is approximately three times that of lipids with the same tails, but a smaller phosphoethanolamine head group, i.e., DLPC versus DLPE, and POPC versus POPE (Table 3). Careful inspection of the free-energy profiles reveals two features that differ significantly in PC versus PE bilayers, namely, (i) the increased barrier height and width, and (ii) the reduced depth of the interfacial valley in the latter bilayers. Both features can be related to bilayer structural differences brought by the variation in the lipid head groups. As shown

in Figure 4, the head group EDP of a PE lipid has a smaller peak compared to PC and PS lipids, consistent with the less bulky head group structure of the former than the latter two. On top of such a size difference, hydrogen bonding capabilities clearly differ among the three head groups (Table 4), with PE and the negatively charged PS forming, on average, an order of magnitude more hydrogen bonds than the PC lipids. The smaller head group of PE along with its greater hydrogen-bonding capability contributes to a significantly smaller APL than the corresponding PC lipids (Table 4), which, in effect, "squeezes out" the free volume within the tail region of a PE bilayer, thereby, widening its PMF barrier, while increasing its height. This difference may also explain the more pronounced interfacial valley in the PMFs for the PC bilayers. Among the six single-lipid bilayers studied here, the influence of the head group is perhaps the most dramatic in the comparison of DLPC versus DLPE, where the carbon EDP of the former bilayer is only half the value of that of the latter (Figure 4). Consistent with such discrepant EDPs, DLPC also exhibits less order than DLPE across the entire acyl chain. The relatively low carbon density in the interfacial region of DLPC facilitates the penetration of water into the lipid bilayer, which may also contribute to lowering the work incurred in ethanol permeation in this region.

Comparing the mammalian membrane with the single-lipid bilayers discussed previously reveals intriguing structural features. For instance, analysis of the average number of hydrogen bonds involving any single lipid in a given configuration indicates that compared with a PC bilayer, the components of the mammalian membrane form much stronger interactions both with one another and with water. Just like in single-lipid bilayers, strong head group interactions tend to produce a densely packed membrane. Indeed, with the exception of DLPE, all six single-lipid bilayers examined here have APL values above 60 $Å^2$, while that of the mammalian membrane is only 50.2 $Å^2$, in line with 51.3 $Å^2$ found using the CG model by Ingólfsson et al.[36] We note, however, that the APL value of the mammalian membrane ought to be interpreted with caution, since its lipid components vary considerably in size. Nonetheless, its carbon EDP shown in Figure 4 reveals that the mammalian membrane is

the most densely packed among all lipid bilayers. These unique structural properties of the mammalian membrane rationalize the similarity of its permeability to ethanol with that of the more densely packed POPE, compared with the commonly used POPC bilayer.

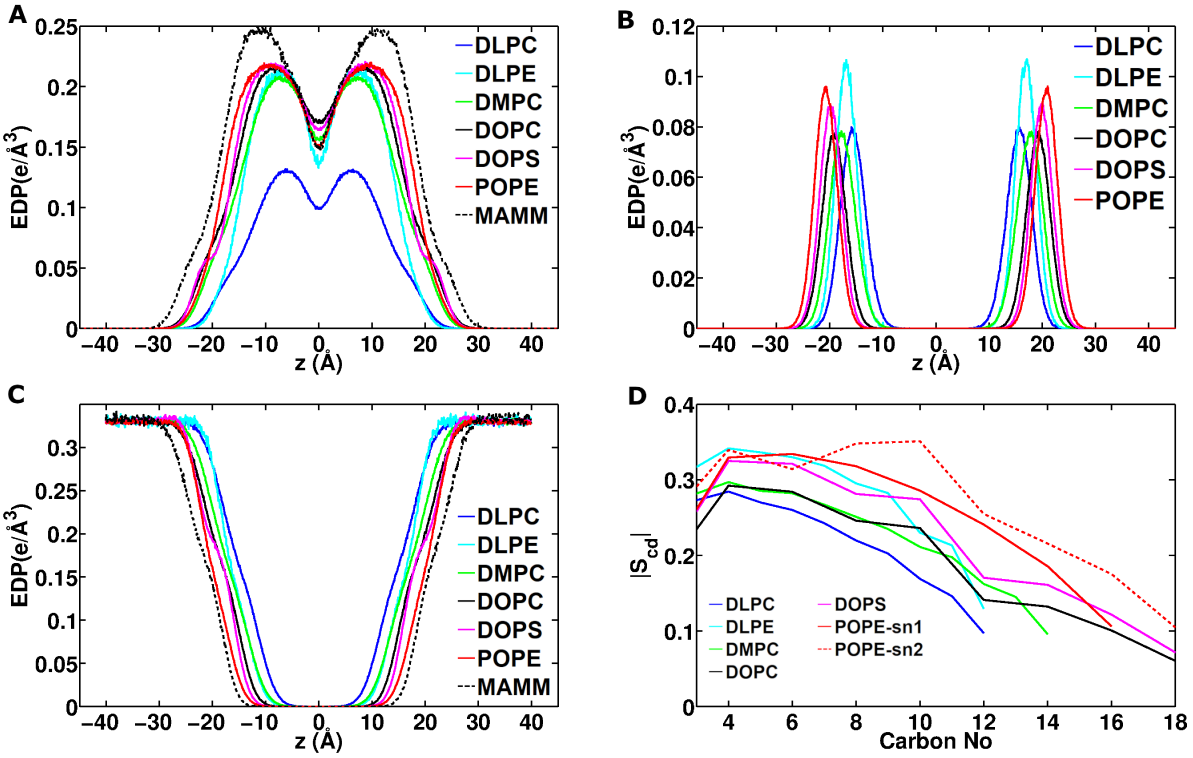

Figure 4: EDP of carbon (A), head group (B) and water (C) as well as the order parameter $|S_{CD}|$ (D) of different lipid bilayer models.

3.4 Membrane permeability to short-chain alcohols estimated via FEP

The free-energy profiles underlying the permeation of short-chain alcohols, namely, methanol, ethanol, 1-propanol and 1-butanol, have been determined using ABF and reported in a previous study.[17] Accurate estimation of the full $w(z)$ function using ABF, or any other importance-sampling algorithm, is computationally costly and the simulation time for the different computational assays ranges between 1.46 and 3.65 μs. Here, we demonstrate that the free-energy profiles of ethanol, 1-propanol and 1-butanol permeation reported previously

Table 4: Average number of hydrogen bonds (H-bond) between lipid and water (L-W) and between lipid molecules (L-L), as well as the area per lipid (APL) of various bilayers studied in this work. Average H-bond number was obtained by first dividing the total L-W or L-L H-bond numbers at a given simulation frame by the number of lipids and then averaging over a given simulation trajectory.

Bilayer	H-bond (L-W)	H-bond (L-L)	APL (Å^2)
DLPC	4.1×10^{-2}	1.2×10^{-2}	66.8
DMPC	4.0×10^{-2}	1.7×10^{-2}	65.4
DOPC	3.9×10^{-2}	1.5×10^{-2}	72.1
DLPE	52.0×10^{-2}	17.3×10^{-2}	58.1
DOPS	41.0×10^{-2}	23.0×10^{-2}	67.9
POPE	52.1×10^{-2}	15.8×10^{-2}	61.1
Mammalian	25.0×10^{-2}	10.3×10^{-2}	50.2

can be recovered using FEP calculations and interpolation. The computational cost for each assay, as shown in Table S3, is significantly reduced, while the estimate of the membrane permeability deviates by no more than 25% from the reference PMF obtained using the ABF algorithm.

The free-energy profile of ethanol permeation inferred from FEP calculations and interpolation, hereon referred to as the low-resolution result, is shown Figure 5 and compared with the PMF from reference 17. The PMF obtained via ABF from reference 17, hereon referred to as the high-resolution result, features a minimum of the free energy around ±13 Å, which corresponds with ethanol molecule being oriented so that its hydroxyl group lies near the lipid head-groups while its hydrophobic ethyl moiety makes contact with the lipid tails.[17] It is worth noting that the value of z at which the FEP calculations were carried out (marked as circle) were intentionally chosen to match the stationary points of the PMF, so that the interpolation can recover its key features with utmost accuracy. The values of z at the barrier and in the valley correspond to a free energy remarkably close to the one obtained using ABF, with a deviation of about 5%. The free energy is, however, somewhat underestimated by 20% at the peak in the head-group region.

The PMF describing 1-propanol permeation was determined by measuring the free-energy difference associated with the mutation of ethanol at the aforementioned five stationary

points. Similarly, the PMF for 1-butanol permeation was obtained through mutation of 1-propanol at each point. Both PMFs are shown in Figure 5. Interestingly enough, the position of the minimum shifted slightly away from the interfacial region as the acyl chain length of the alcohol increased, evolving from 14 Å for ethanol to 12 Å for 1-butanol. It is also noteworthy that although we performed extensive sampling to ensure the quality of the FEP calculations (200 ns at a given value of z), convergence was in fact well achieved within 40 ns (Figure S4).

The approximated diffusivity profiles describing short-chain alcohols are shown in the bottom row of Figure 5, which reveals a good agreement with the fractional diffusivity profiles obtained in reference 17. The calculated permeability values, using the PMFs obtained via FEP and the approximate diffusivity profiles, are shown in Table 5. For ethanol, the P_m value obtained by the above approximate, low-resolution method (P_{m} (Low-resolution) in Table 5) shows the least deviation from that obtained with the ABF and fractional diffusivity profiles (P_{m} (High-resolution) in Table 5), with a difference of 13%. 1-propanol, on the other hand, shows a larger deviation of 25%. The estimated permeability does not appear to be overly sensitive to the choice of the sampling points used in the FEP calculation. For instance, shifting the FEP sampling point at the valley region of the PMF from 13 Å to 15 Å, results in permeability values (P_{m} (Low-resolution, shifted) in Table 5) that differ by roughly 5% from the P_{m} (Low-resolution) result.

Table 5: Calculated permeability P_{m} (unit: cm/s) of ethanol, propanol and butanol in POPC using ABF ("High-resolution") and FEP ("Low-resolution"). FEP calculations were performed at $z = 15$ Å instead of $z = 13$ Å for the "Low-resolution, shifted" result.

Alcohol	P_{m} (High-resolution)	P_{m} (Low-resolution)	P_{m} (Low-resolution, shifted)
Ethanol	0.81	0.71	0.68
Propanol	2.31	1.73	1.69
Butanol	7.30	5.84	5.60

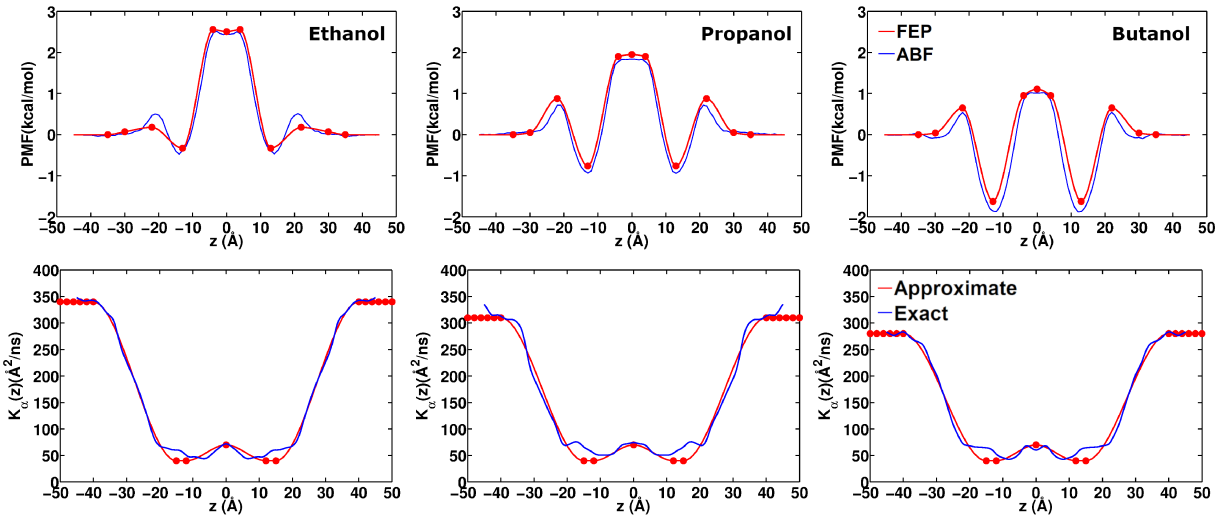

Figure 5: PMF (top) and diffusivity profiles (bottom) of ethanol in POPC. For PMFs, the ABF results (blue) were obtained from Comer and Chipot,[17] while FEP calculations were performed at selected points (red dots) and subsequently used to generate the PMFs (red curves) via interpolation. For diffusivity, the fractional diffusivity (blue) were from Comer and Chipot ,[17] while the red curves represent approximate diffusivity profiles obtained from bulk diffusivity values via interpolation.

4 Conclusions

In this contribution, we have examined how the chemical nature of the lipid impacts the membrane permeability to small molecules determined from first principles. Toward this end, we have considered six computational assays consisting of single-lipid bilayers, exploring the role played by the acyl-chain length and the size of the head group on the permeation events, and compared the latter with the results obtained using a 26-component mammalian membrane. We have found that the seven estimates of the membrane permeability fall within an order of magnitude, remembering that typically, theoretical predictions of the membrane permeability are within an order of magnitude to experimental value,[11] which can be ascribed to a variety of sources of error ranging from force-field inaccuracies to sampling incompleteness. We conclude that at a qualitative level, homogeneous single-lipid bilayers can provide a reasonable model of the heterogeneous mammalian membrane, with the caveat that combination of extremely short-tail lipids endowed with a bulky head group ought to

be avoided. At a quantitative level, the free-energy landscapes can be markedly different from two distinct standpoints. On the one hand, short-tail lipids yield a narrow barrier in the hydrophobic region. On the other hand, the bulkier head groups of PC and PS lipids result in a more pronounced free-energy dip beneath the interfacial region.

Among the six single-lipid bilayers examined here, the membrane permeability estimate provided by POPE provides the best agreement with the reference mammalian membrane. In contrast, the membrane permeability obtained previously in POPC[17] is over six times greater than that of the mammalian membrane. Thus, for the membrane permeability estimation of small alcohols, the mammalian membrane is in fact best mimicked by a single-species bilayer with a relatively small lipid head group. Given that PC lipids constitute the most abundant phospholipid species in a mammalian membrane,[65] this behavior is somewhat surprising. It is likely explained by the presence of cholesterol as well as various charged lipid species, which effectively "condense" the mammalian membrane, rendering it in closer resemblance to a PE bilayer with relatively small lipid head groups. Therefore, while a mixed, heterogeneous membrane still provides the best approximation to a mammalian membrane, if a single-lipid bilayer has to be adopted in permeability estimation, a POPE bilayer appears to be a better candidate than the more commonly used POPC. One legitimate question that arises from the investigation of permeation events, most notably with a mammalian membrane model, is the convergence of the free-energy calculation. In particular, it remains unclear whether the permeant interacted with all the components of the membrane on the timescale of our simulation. Inspection of the trajectory shows diffusion throughout x, y–plane that over the range of z values explored within the allotted time of 3.6 μs, though satisfying this necessary condition may not be sufficient to guarantee the correct reproduction of the membrane permeability to the short-chain alcohol. In the context of modeling permeation events, it is of paramount importance to correctly describe the membrane structure, which can be partially characterized by the average area per lipid. The area per lipid has been recognized to correlate with the membrane permeability[66] — a criterion that in light of the

data of Ingólfsson et al.[36] appears to be met in our simulations.

At the core of theoretical predictions of the membrane permeability to small molecules, evaluation of the potential of mean force that underlies the permeation event represents the bulk of the computational investment. Imposing a maximum hysteresis of about $k_{\mathrm{B}}T$ across the entire reaction pathway, i.e., 90 Å, results in simulation times ranging from 2.5 to 4.5 μs, which roughly corresponds to 3–5 days of computation on a commodity cluster equipped with latest-generation graphics cards. These staggering wall-clock times preclude high-throughput screening of large sets of permeants, and are, therefore, incompatible with the requirements of drug discovery in nonacademic environments, thus, providing a rationale for turning to approximate approaches. The similar features of the position-dependent diffusivity profiles and potentials of mean force obtained for a congeneric series of substrates permeating the same homogeneous, single-lipid bilayer further suggest that these curves can be modeled from the knowledge of their stationary points. Here, we have shown that the potential of mean force characterizing permeation can be described without perceptible loss of resolution by five points corresponding to distinct values of z, whereby the substrate is coupled reversibly to its environment, employing bidirectional FEP calculations. Hence, with a very modest computational investment of 40 ns per point, that is 0.2 μs per permeant, the effective cost of a potential of mean force is reduced by an order of magnitude compared to a conventional computation of the full potential of mean force. Moreover, we have modeled the position-dependent diffusivity profiles by means of a simple sigmoid function, leaning on the theoretical estimate of the self-diffusion of the permeant in a bulk aqueous environment. Investigation of ethanol permeation indicates that the membrane permeability determined following an approximate strategy falls within 25% from the reference quantity obtained from ABF simulations and Bayesian inferences. Deviation from the reference membrane permeability stems primarily from offset maxima and minima in the fitted potential of mean force compared with the ABF free-energy profile, but can be reduced at the price of introducing additional points along the transition coordinate, z, and running FEP calculations at these

points. Although compromising between cost and accuracy is necessary to reconcile the modeled free-energy profile with that supplied by a full-fledged ABF calculation, a modest computational investment appears to be sufficient for the purpose of ranking substrates with respect to their membrane permeability. Reliability of the approximate strategy remains, however, contingent on presumptive knowledge of the stationary points of the free-energy landscape, which, to a large extent, constitute a signature of the lipid bilayer.

In pharmaceutical development, one is generally more interested in ranking drug candidates according to specific properties, e.g., their binding affinity towards a target protein, than in absolute quantities, which rationalizes the popularity of relative free-energy calculations in drug discovery. Under these premises, we have proposed a natural extension of the FEP-based approximate strategy to determine the relative membrane permeability between different permeants. At the stationary points of the free-energy landscape, instead of coupling it reversibly from the environment, the substrate is transformed alchemically into an alternate one by means of FEP calculations. Mapping the potential of mean force underlying permeation of a reference substrate is recommended for proper estimation of the values of z at which point mutations will be performed, because the latter will be utilized to recover the free-energy profile of the alternate substrate. Successive alchemical transformation of ethanol into 1-propanol and 1-butanol underscores that while the membrane permeability departs somewhat from the reference quantity determined from first principles, its increase with the length of the alkyl chain is suitably reproduced, which should be appropriate for drug-ranking purposes. Moreover, the present approximate strategy may prove advantageous for bulky substrates that only differ by one functional group, in which event calculation of the potential of mean force underlying permeation constitutes an insuperable obstacle for the study of large sets of permeants. Considering the affordable computational investment of 40 ns per point, that is 0.2 μs per permeant, it represents an appealing, viable alternative to a rigorous approach resting on explicit mapping of the PMF coupled with Bayesian inference of the diffusivity.

Acknowledgement

C.H.T., S.K.S.C. and Y.W. are supported by Project 14323816 from the Research Grants Council. Y.W. and C.C. acknowledge the France-Hong Kong Programme Hubert Curien (PHC) Procore for funding. Some computing for this project was performed on the Beocat Research Cluster at Kansas State University, which is funded in part by NSF grants CHE-1726332, CNS-1006860, EPS-1006860, and EPS-0919443. C. C. is grateful to the Contrat Plan État Région (CPER) IT2MP and to the Fonds Européen de Développement en Région (FEDER) for generous funding, and to the Centre National de la Recherche Scientifique for the support of a joint research program (PICS) with China. Y.W. also acknowledges Project 21403183 from the National Natural Science Foundation of China and direct grant support from the Chinese University of Hong Kong.

References

(1) Subczynski, W. K.; Hyde, J. S.; Kusumi, A. Oxygen permeability of phosphatidylcholine–cholesterol membranes. *Proceedings of the National Academy of Sciences* **1989**, *86*, 4474–4478.

(2) Missner, A.; Kügler, P.; Saparov, S. M.; Sommer, K.; Matthai, J. C.; Zeidel, M. L.; Pohl, P. Carbon dioxide transport through membranes. *Journal of Biological Chemistry* **2008**, *283*, 25340–25347.

(3) Subczynski, W. K.; Lomnicka, M.; Hyde, J. S. Permeability of nitric oxide through lipid bilayer membranes. *Free Radical Research* **1996**, *24*, 343–349.

(4) Mathai, J. C.; Missner, A.; Kügler, P.; Saparov, S. M.; Zeidel, M. L.; Lee, J. K.; Pohl, P. No facilitator required for membrane transport of hydrogen sulfide. *Proceedings of the National Academy of Sciences* **2009**, *106*, 16633–16638.

(5) Giorgi, E.; Stein, W. The transport of steroids into animal cells in culture. *Endocrinology* **1981**, *108*, 688–697.

(6) Dobson, P. D.; Kell, D. B. Carrier-mediated cellular uptake of pharmaceutical drugs: an exception or the rule? *Nature reviews Drug Discovery* **2008**, *7*, 205.

(7) Kell, D. B.; Dobson, P. D.; Oliver, S. G. Pharmaceutical drug transport: the issues and the implications that it is essentially carrier-mediated only. *Drug Discovery Today* **2011**, *16*, 704–714.

(8) Matsson, P.; Fenu, L. A.; Lundquist, P.; Wiśniewski, J. R.; Kansy, M.; Artursson, P. Quantifying the impact of transporters on cellular drug permeability. *Trends in Pharmacological Sciences* **2015**, *36*, 255–262.

(9) Tsaioun, K.; Bottlaender, M.; Mabondzo, A. ADDME – Avoiding Drug Development Mistakes Early: central nervous system drug discovery perspective. *BMC Neurology* **2009**, *9*, S1.

(10) Awoonor-Williams, E.; Rowley, C. N. Molecular simulation of nonfacilitated membrane permeation. *Biochimica et Biophysica Acta (BBA)-Biomembranes* **2016**, *1858*, 1672–1687.

(11) Tse, C. H.; Comer, J.; Wang, Y.; Chipot, C. Link between Membrane Composition and Permeability to Drugs. *Journal of Chemical Theory and Computation* **2018**, *14*, 2895–2909.

(12) Marrink, S.-J.; Berendsen, H. J. C. Simulation of water transport through a lipid membrane. *The Journal of Physical Chemistry* **1994**, *98*, 4155–4168.

(13) Diamond, J. M.; Katz, Y. Interpretation of nonelectrolyte partition coefficients between dimyristoyl lecithin and water. *The Journal of Membrane Biology* **1974**, *17*, 121–154.

(14) Chipot, C., Pohorille, A., Eds. *Free energy calculations. Theory and applications in chemistry and biology*; Springer Verlag: Berlin, Heidelberg, New York, 2007.

(15) Chipot, C. Frontiers in free-energy calculations of biological systems. *Wiley Interdiscip. Rev. Comput. Mol. Sci.* **2014**, *4*, 71–89.

(16) Chipot, C.; Comer, J. Subdiffusion in Membrane Permeation of Small Molecules. *Scientific Reports* **2016**, *6*.

(17) Comer, J.; Schulten, K.; Chipot, C. Permeability of a Fluid Lipid Bilayer to Short-Chain Alcohols from First Principles. *Journal of Chemical Theory and Computation* **2017**, *13*, 2523–2532.

(18) Marrink, S.; Berendsen, H. Permeation Process of Small Molecules across Lipid Membranes Studied by Molecular Dynamics Simulations. *Journal of Physical Chemistry* **1996**, *100*, 16729–38.

(19) Riahi, S.; Rowley, C. N. Why can hydrogen sulfide permeate cell membranes? *Journal of the American Chemical Society* **2014**, *136*, 15111–15113.

(20) Bemporad, D.; Luttmann, C.; Essex, J. Computer Simulation of Small Molecule Permeation across a Lipid Bilayer: Dependence on Bilayer Properties and Solute Volume, Size, and Cross-Sectional Area. *Biophysical Journal* **2004**, *87*, 1–13.

(21) Hulbert, A.; Rana, T.; Couture, P. The acyl composition of mammalian phospholipids: an allometric analysis. *Comparative Biochemistry and Physiology Part B: Biochemistry and Molecular Biology* **2002**, *132*, 515–527.

(22) Comer, J.; Schulten, K.; Chipot, C. Calculation of Lipid-Bilayer Permeabilities Using an Average Force. *Journal of Chemical Theory and Computation* **2014**, *10*, 554–564.

(23) Ghysels, A.; Venable, R. M.; Pastor, R. W.; Hummer, G. Position-Dependent Diffusion

Tensors in Anisotropic Media from Simulation: Oxygen Transport in and through Membranes. *Journal of Chemical Theory and Computation* **2017**, *13*, 2962–2976.

(24) Ghaemi, Z.; Minozzi, M.; Carloni, P.; Laio, A. A novel approach to the investigation of passive molecular permeation through lipid bilayers from atomistic simulations. *Journal of Physical Chemistry B* **2012**, *116*, 8714–8721.

(25) Comer, J.; Schulten, K.; Chipot, C. Diffusive Models of Membrane Permeation with Explicit Orientational Freedom. *Journal of Chemical Theory and Computation* **2014**, *10*, 2710–2718.

(26) Wei, C.; Pohorille, A. Permeation of nucleosides through lipid bilayers. *Journal of Physical Chemistry B* **2011**, *115*, 3681–3688.

(27) Neale, C.; Madill, C.; Rauscher, S.; Pomès, R. Accelerating Convergence in Molecular Dynamics Simulations of Solutes in Lipid Membranes by Conducting a Random Walk along the Bilayer Normal. *Journal of Chemical Theory and Computation* **2013**, *9*, 3686–3703.

(28) Lee, C. T.; Comer, J.; Herndon, C.; Leung, N.; Pavlova, A.; Swift, R. V.; Tung, C.; Rowley, C. N.; Amaro, R. E.; Chipot, C.; Wang, Y.; Gumbart, J. C. Simulation-Based Approaches for Determining Membrane Permeability of Small Compounds. *Journal of Chemical Information and Modeling* **2016**, *56*, 721–733.

(29) Ghaemi, Z.; Alberga, D.; Carloni, P.; Laio, A.; Lattanzi, G. Permeability Coefficients of Lipophilic Compounds Estimated by Computer Simulations. *Journal of Chemical Theory and Computation* **2016**, *12*, 4093–4099.

(30) Sun, R.; Han, Y.; Swanson, J. M.; Tan, J. S.; Rose, J. P.; Voth, G. A. Molecular transport through membranes: Accurate permeability coefficients from multidimensional potentials of mean force and local diffusion constants. *The Journal of Chemical Physics* **2018**, *149*, 072310.

(31) Cardenas, A. E.; Jas, G. S.; DeLeon, K. Y.; Hegefeld, W. A.; Kuczera, K.; Elber, R. Unassisted transport of N-acetyl-L-tryptophanamide through membrane: experiment and simulation of kinetics. *Journal of Physical Chemistry B* **2012**, *116*, 2739–2750.

(32) Tu, K.; Klein, M.; Tobias, D. J. Constant-pressure molecular dynamics investigations of cholesterol effects in a dipalmitoylphosphatidylcholine bilayer. *Biophysical Journal* **1998**, *75*, 2147–2156.

(33) Smondyrev, A. M.; Berkowitz, M. L. Structure of dipalmitoylphosphatidylcholine/cholesterol bilayer at low and high cholesterol concentrations: molecular dynamics simulation. *Biophysical Journal* **1999**, *77*, 2075–2089.

(34) Murzyn, K.; Róg, T.; Pasenkiewicz-Gierula, M. Phosphatidylethanolamine-phosphatidylglycerol bilayer as a model of the inner bacterial membrane. *Biophysical Journal* **2005**, *88*, 1091–1103.

(35) Hoopes, M. I.; Noro, M. G.; Longo, M. L.; Faller, R. Bilayer structure and lipid dynamics in a model stratum corneum with oleic acid. *The Journal of Physical Chemistry B* **2011**, *115*, 3164–3171.

(36) Ingólfsson, H. I.; Melo, M. N.; Van Eerden, F. J.; Arnarez, C.; Lopez, C. A.; Wassenaar, T. A.; Periole, X.; De Vries, A. H.; Tieleman, D. P.; Marrink, S. J. Lipid organization of the plasma membrane. *Journal of the American Chemical Society* **2014**, *136*, 14554–14559.

(37) Wu, E. L.; Cheng, X.; Jo, S.; Rui, H.; Song, K. C.; Dávila-Contreras, E. M.; Qi, Y.; Lee, J.; Monje-Galvan, V.; Venable, R. M.; Klauda, J. B.; Im, W. CHARMM-GUI membrane builder toward realistic biological membrane simulations. *Journal of Computational Chemistry* **2014**, *35*, 1997–2004.

(38) Rivel, T.; Ramseyer, C.; Yesylevskyy, S. Permeation of cisplatin through the membranes of normal and cancer cells: a molecular dynamics study. *bioRxiv* **2018**, 375980.

(39) Mori, T.; Miyashita, N.; Im, W.; Feig, M.; Sugita, Y. Molecular dynamics simulations of biological membranes and membrane proteins using enhanced conformational sampling algorithms. *Biochimica et Biophysica Acta (BBA)-Biomembranes* **2016**, *1858*, 1635–1651.

(40) Parisio, G.; Stocchero, M.; Ferrarini, A. Passive membrane permeability: beyond the standard solubility-diffusion model. *Journal of Chemical Theory and Computation* **2013**, *9*, 5236–5246.

(41) Landau, L. D. *Statistical Physics*; Clarendon Press: Oxford, 1938.

(42) Zwanzig, R. W. High-Temperature Equation of State by a Perturbation Method. I. Nonpolar Gases. *The Journal of Chemical Physics* **1954**, *22*, 1420–1426.

(43) Hummer, G. Position-dependent diffusion coefficients and free energies from Bayesian analysis of equilibrium and replica molecular dynamics simulations. *New Journal of Physics* **2005**, *7*, 34–34.

(44) Comer, J.; Chipot, C.; González-Nilo, F. D. Calculating Position-Dependent Diffusivity in Biased Molecular Dynamics Simulations. *Journal of Chemical Theory and Computation* **2013**, *9*, 876–882.

(45) Comer, J. Calculate position-dependent diffusivity functions from trajectory data. `https://github.com/jeffcomer/DiffusionFusion`, 2016.

(46) Comer, J.; Gumbart, J. C.; Hénin, J.; Lelièvre, T.; Pohorille, A.; Chipot, C. The Adaptive Biasing Force Method: Everything You Always Wanted To Know but Were Afraid To Ask. *The Journal of Physical Chemistry B* **2015**, *119*, 1129–1151.

(47) Crank, J.; Nicolson, P.; Hartree, D. R. A practical method for numerical evaluation of solutions of partial differential equations of the heat-conduction type. *Mathematical Proceedings of the Cambridge Philosophical Society* **1947**, *43*, 50.

(48) Murio, D. A. Implicit finite difference approximation for time fractional diffusion equations. *Computers & Mathematics with Applications* **2008**, *56*, 1138–1145.

(49) Sweilam, N.; Khader, M.; Mahdy, A. Crank-Nicolson finite difference method for solving time-fractional diffusion equation. *Journal of Fractional Calculus and Applications* **2012**, *2*, 1–9.

(50) Phillips, J. C.; Braun, R.; Wang, W.; Gumbart, J.; Tajkhorshid, E.; Villa, E.; Chipot, C.; Skeel, R. D.; Kalé, L.; Schulten, K. Scalable molecular dynamics with NAMD. *Journal of Computational Chemistry* **2005**, *26*, 1781–1802.

(51) Klauda, J. B.; Venable, R. M.; Freites, J. A.; O'Connor, J. W.; Tobias, D. J.; Mondragon-Ramirez, C.; Vorobyov, I.; MacKerell, A. D.; Pastor, R. W. Update of the CHARMM All-Atom Additive Force Field for Lipids: Validation on Six Lipid Types. *The Journal of Physical Chemistry B* **2010**, *114*, 7830–7843.

(52) Jorgensen, W. L.; Chandrasekhar, J.; Madura, J. D.; Impey, R. W.; Klein, M. L. Comparison of simple potential functions for simulating liquid water. *The Journal of Chemical Physics* **1983**, *79*, 926–935.

(53) Feller, S. E.; Zhang, Y.; Pastor, R. W.; Brooks, B. R. Constant pressure molecular dynamics simulation: The Langevin piston method. *The Journal of Chemical Physics* **1995**, *103*, 4613–4621.

(54) Andersen, H. C. Rattle: A "velocity" version of the shake algorithm for molecular dynamics calculations. *Journal of Computational Physics* **1983**, *52*, 24–34.

(55) Miyamoto, S.; Kollman, P. A. Settle: An analytical version of the SHAKE and RATTLE algorithm for rigid water models. *Journal of Computational Chemistry* **1992**, *13*, 952–962.

(56) Tuckerman, M.; Berne, B. J.; Martyna, G. J. Reversible multiple time scale molecular dynamics. *The Journal of Chemical Physics* **1992**, *97*, 1990–2001.

(57) Darve, E.; Pohorille, A. Calculating free energies using average force. *The Journal of Chemical Physics* **2001**, *115*, 9169–9183.

(58) Hénin, J.; Chipot, C. Overcoming free energy barriers using unconstrained molecular dynamics simulations. *The Journal of Chemical Physics* **2004**, *121*, 2904–2914.

(59) Darve, E.; Rodríguez-Gómez, D.; Pohorille, A. Adaptive biasing force method for scalar and vector free energy calculations. *The Journal of Chemical Physics* **2008**, *128*, 144120.

(60) Holte, L. L.; Gawrisch, K. Determining ethanol distribution in phospholipid multilayers with MAS-NOESY spectra. *Biochemistry* **1997**, *36*, 4669–4674.

(61) Ly, H. V.; Longo, M. L. The influence of short-chain alcohols on interfacial tension, mechanical properties, area/molecule, and permeability of fluid lipid bilayers. *Biophysical Journal* **2004**, *87*, 1013–1033.

(62) Mathai, J. C.; Tristram-Nagle, S.; Nagle, J. F.; Zeidel, M. L. Structural Determinants of Water Permeability through the Lipid Membrane. *The Journal of General Physiology* **2008**, *131*, 69–76.

(63) Brahm, J. Diffusional water permeability of human erythrocytes and their ghosts. *The Journal of General Physiology* **1982**, *79*, 791–819.

(64) Brahm, J. Permeability of human red cells to a homologous series of aliphatic alcohols. Limitations of the continuous flow-tube method. *The Journal of General Physiology* **1983**, *81*, 283–304.

(65) Van Meer, G.; Voelker, D. R.; Feigenson, G. W. Membrane lipids: where they are and how they behave. *Nature reviews Molecular cell biology* **2008**, *9*, 112.

(66) Shinoda, W. Permeability across lipid membranes. *Biochimica et Biophysica Acta (BBA) - Biomembranes* **2016**, *1858*, 2254–2265.

Supporting Information

Table S1: Equilibration time of systems initiated from different snapshots of the SMD trajectory. z refers to the Euclidean distance between center of mass of the permeant to the center of a lipid bilayer projected along the membrane normal.

z (Å)	Equilibration time (ns)
±35	10
±30	25
±20	50
±10	100
0	100

Table S2: Composition of the mammalian membrane model simulated in this work. The membrane contains altogether 26 types of components, with 127 and 129 molecules in its upper and lower leaflet, respectively. Lipid names correspond to residue names used by the CHARMM36 force field.

Lipid	No. (upper leaflet)	No. (lower leaflet)
ASM	1	2
CER241	0	1
CHL1	38	43
DAPE	6	1
DOPC	1	1
DOPE	3	1
LSM	2	3
NSM	6	12
OSM	0	1
PLPC	12	26
PLPE	7	2
PLPS	2	0
POPA	1	0
POPC	8	17
POPE	8	2
POPI14	1	0
POPI2A	1	0
POPI33	1	0
POPS	3	0
PSM	4	9
SAPC	2	4
SAPE	7	2
SAPS	7	0
SDPC	0	1
SDPE	3	1
SDPS	3	0

Table S3: Computation time for FEP calculations of short-chain alcohols. Each FEP calculation was performed in 20 windows, during which the coupling parameter λ was varied from 0 to 1. We simulated each window for 10 ns, resulting in a total of 200 ns for the FEP calculation at a given z.

z (Å)	Total simulation time (ns)
0	200
4	200
13	200
22	200
30	200
Aggregate simulate time (μs) 1	

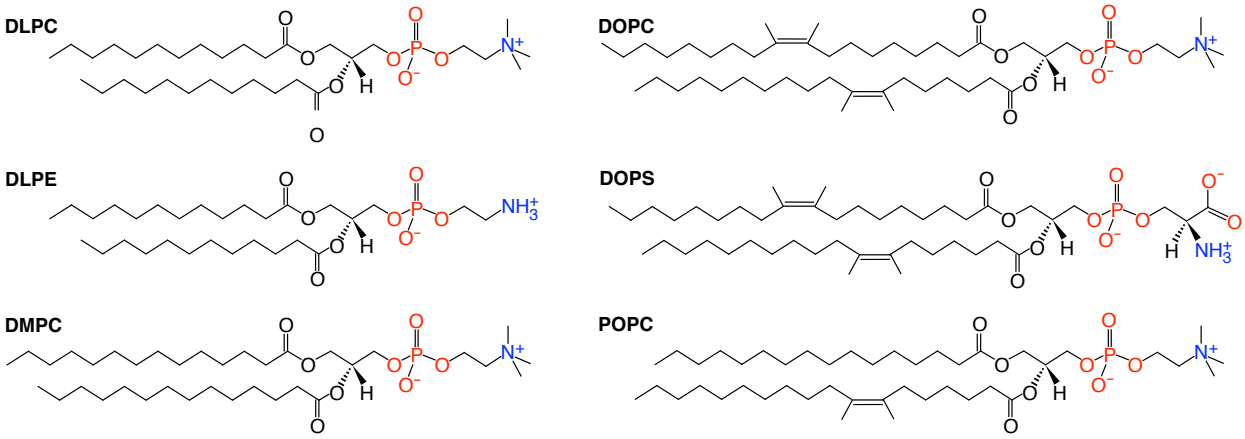

Figure S1: Chemical structures of molecules from six single-species lipid bilayers studied in this work.

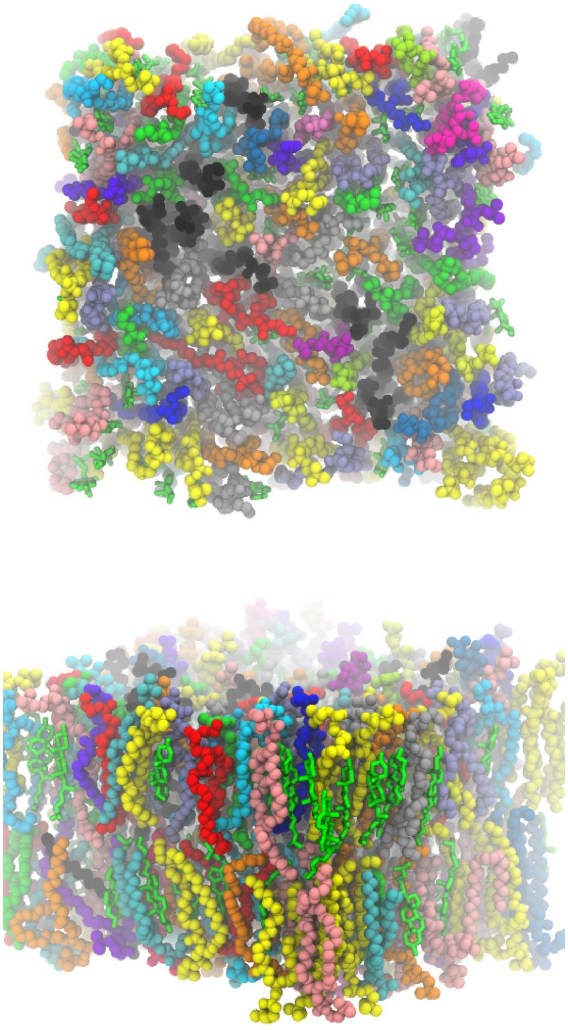

Figure S2: Top (top) and side (bottom) views of the all-atom mammalian membrane model. For clarity, water and ions were not shown.

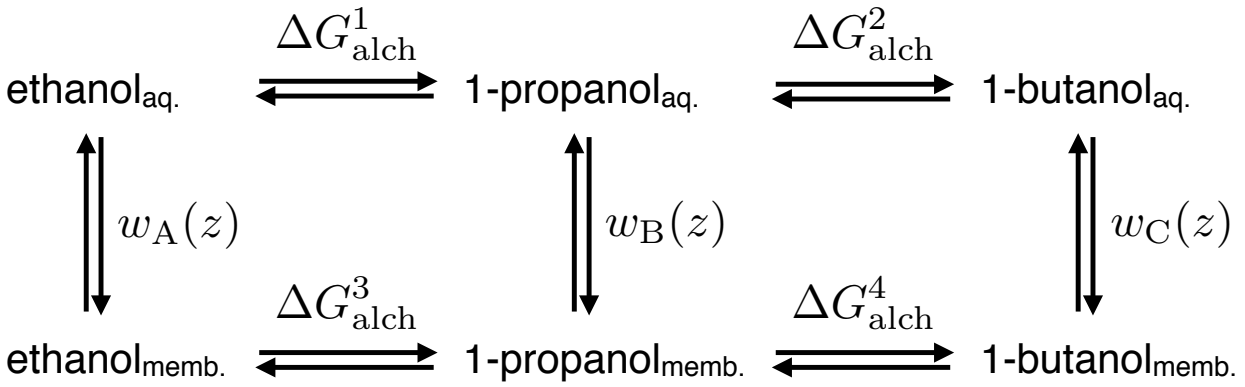

Figure S3: Thermodynamic cycle of short-chain alcohol mutation. The subscripts 'aq' and 'memb' stand for the aqueous solution and the lipid membrane, respectively.

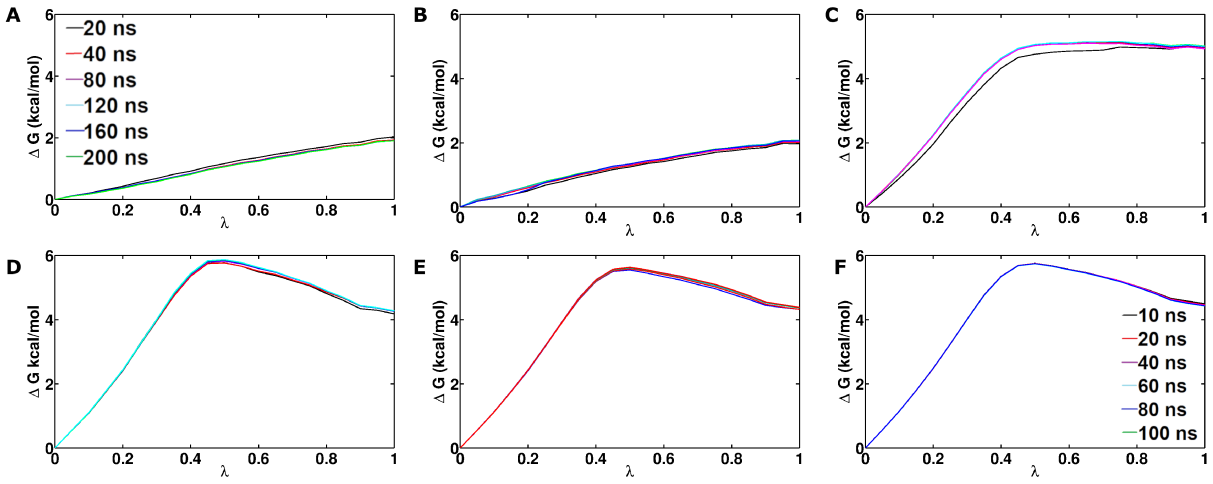

Figure S4: Convergence of FEP calculations indicated by free energy change (ΔG) of ethanol annihilation in various locations ($z = 0$ Å (A), $z = 4$ Å (B), $z = 13$ Å (C), $z = 22$ Å (D), $z = 30$ Å (E)) within the POPC membrane system and in bulk water (F) as the amount of sampling increases. At a given z within the membrane system, FEP was performed in 20 windows with 10-ns sampling in each window. In bulk water, FEP was performed in 20 windows with 5-ns sampling in each window. The sampling amount indicated by the curves represent the total amount of sampling in a FEP calculation, i.e., up to $20\times10 = 200$ ns for a given z location within the membrane system (A-E) and up to $20\times5 = 100$ ns for bulk water (F).